



UNIVERSITÀ POLITECNICA DELLE MARCHE
Repository ISTITUZIONALE

Combination of reaction synthesis and Spark Plasma Sintering in production of Ti-Al-Si alloys

This is a pre print version of the following article:

Original

Combination of reaction synthesis and Spark Plasma Sintering in production of Ti-Al-Si alloys / Knaislová, A.; Novák, P.; Cabibbo, M.; Filip, Prusa; Paoletti, C.; Jaworska, L.; Vojtěch, D.. - In: JOURNAL OF ALLOYS AND COMPOUNDS. - ISSN 0925-8388. - ELETTRONICO. - 752:5(2018), pp. 317-326.
[10.1016/j.jallcom.2018.04.187]

Availability:

This version is available at: 11566/258645 since: 2022-06-15T19:12:03Z

Publisher:

Published

DOI:10.1016/j.jallcom.2018.04.187

Terms of use:

The terms and conditions for the reuse of this version of the manuscript are specified in the publishing policy. The use of copyrighted works requires the consent of the rights' holder (author or publisher). Works made available under a Creative Commons license or a Publisher's custom-made license can be used according to the terms and conditions contained therein. See editor's website for further information and terms and conditions.

This item was downloaded from IRIS Università Politecnica delle Marche (<https://iris.univpm.it>). When citing, please refer to the published version.

(Article begins on next page)

Combination of reaction synthesis and Spark Plasma Sintering in production of Ti-Al-Si alloys

A. Knaislová^{1*}, P. Novák¹, M. Cabibbo², F. Průša¹, C. Paoletti², L. Jaworska³

¹Department of Metals and Corrosion Engineering, University of Chemistry and Technology, Prague.
Technická 5, 166 28 Prague. Czech Republic.

²DIISM/Università Politecnica delle Marche, Via Brecce Bianche, 60131 Ancona. Italy.

³The Institute of Advanced Manufacturing Technology, Wroclawska 37A, 30-011 Krakow. Poland.

*corresponding author, E-mail: knaisloa@vscht.cz

Abstract

This work is devoted to the preparation of alloys based on intermetallic compounds in Ti-Al-Si system by powder metallurgy using Self-propagating High-temperature Synthesis (SHS). Since samples after SHS are very porous, in order to reduce the porosity, a combination of SHS, milling, and Spark Plasma Sintering (SPS), has been here tested as a complex production technology. Selected mechanical properties of consolidated samples (hardness, fracture toughness) and tribological properties (abrasive wear resistance) were determined. Microstructure of compacted Ti-Al-Si alloys is almost non-porous with the combination of titanium aluminides and titanium silicides. The alloys achieve good mechanical properties except for the fracture toughness.

Keywords: intermetallics, titanium aluminides, titanium silicides, microstructure, X-ray diffraction

1. Introduction

Automotive and aerospace industries are searching for new high-temperature structural materials with improved properties (especially resistance to oxidation, thermal stability and mechanical properties) in combination with low density [1]. Intermetallic compounds based on the Ti-Al system are very attractive

materials, where the decisive factor is low weight of the components. TiAl and Ti₃Al are the most popular titanium aluminides, which are characterised by high resistance against oxidation, creep resistance and low density. γ -TiAl has excellent mechanical properties (relatively high yield strength at elevated temperatures) and corrosion resistance at temperatures above 600 °C. This combination of useful properties makes them very promising high-temperature structural materials [2,3]. Improvement of their mechanical properties can be achieved by the means of alloying e.g. by following elements: silicon (increases strength), chromium and molybdenum (increase resistance against oxidation at high temperatures) or niobium (increases ductility and resistance against oxidation at high temperatures) [4]. Silicon probably seems to be the most promising among these elements because of low density in comparison with chromium, molybdenum or tungsten and the the formation of Ti₅Si₃ phase, which has a significant strengthening effect. Silicon is also appropriate additive for the improvement of the resistance against oxidation and corrosion at high temperatures [5,6].

High brittleness at room temperature is the main drawback of the Ti-Al-Si alloy system, which is likely to be solved by modifying the resulting structure through an appropriate and dedicated, processing technology [7,8]. Very complicated production limits wider use of intermetallics. Conventional melting metallurgy is the most common preparation method of intermetallic compounds nowadays. The use of this method causes serious obstacles because of high melting points of intermediary phases (Ti₅Si₃ melts above 2000 °C), the exothermic reaction during their formation, and high reactivity of the melt with crucible [9]. The other problem is frequent occurrence of casting defects, in particular the formation of cracks and pores, and poor melts fluidity [5]. Forming of intermetallics is almost impossible due to the high brittleness (low toughness) of intermetallic phases and easy cracks formation on surface or in volume of the casting [10].

Reactive sintering appears to be a very suitable method for the production of intermetallics. Mixture of metal powders is compressed and heated to a temperature lower than the melting point of the produced material during this process, which leads to the formation of intermetallic compounds. These reactions are very exothermic. After reaching the initiation temperature of the reaction, there is not necessary to heat up further, reaction proceeds spontaneously using its own energy and it is very fast (max. few minutes). Therefore the process is called Self-propagating High-temperature Synthesis (SHS). For certain alloy systems (e.g. Ti-Al, Fe-Al), porous products are formed by this process [11,12]. Reaction forming Ti-Al intermetallics occurs around 660 °C. Melt is formed from powders of titanium and aluminium at this

temperature. Melt fills some pores, but resulting alloy is still very porous due to unbalanced diffusion rates, high speed and short time of sintering, gas evolution from volatile impurities or possible differences in density of the initial components and reaction products. Addition of silicon could be a solution for this problem. Eutectic Al-Si melt is formed during sintering, which fills the pores and minimizes formation of Kirkendall porosity [7,8,11].

Spark Plasma Sintering (SPS) is a modern way of sintering, which allows creation of compact material from powders by using high heating rate (to more than 300 °C/min) and short-time sintering (usually 5 to 10 minutes). Adsorbed gases and surface oxides on the powder particles are partially removed by spark discharges, which together with high pressure cause a perfect sintering of the material [13]. The sintering temperatures range from few hundreds to above than 2000 °C [14]. The advantage of this sintering method is to maintain the fine-grain structure, to limit the crystallization processes (activated by increasing temperature during sintering) and to gain non-porous solid material [13].

The aim of this study was to prepare innovative materials, based on a Ti-Al-Si system, by using a complex processing technology, such as a sequence of SHS, milling, and Spark Plasma Sintering. This process has a good potential to substitute conventional melting metallurgy for these alloys in the future. The aim of this work is to determine the phase composition, microstructure and selected mechanical properties (especially hardness).

2. Material and methods

2.1. The material

Ti-Al-Si alloys were prepared by powder metallurgy, where at first titanium powder (purity 99.8 %, particle size < 100 µm), silicon powder (purity 99.99 %, particle size < 20 µm) and powder from AlSi30 alloy (particle size of about 100-500 µm) were blended together. Powder (in the form of fine chips) of AlSi30 alloy was prepared by mechanical machining of compact AlSi30 alloy. Then the mixture was compressed by the pressure of 420 MPa at laboratory temperature using a universal loading machine LabTest 5.250SP1-VM. Formed cylindrical samples had a diameter of about 12 mm and height of approx. 6 mm. Pre-pressed samples were sealed in evacuated silica glass ampoules in this process in order to proceed the SHS under vacuum.

2.2. Production method of the intermetallic compound

SHS of pre-pressed powder mixtures TiAl10Si20, TiAl10Si30, TiAl15Si15, TiAl20Si20, TiAl20Si30 and TiAl30Si20 (percentage by weight) was conducted for 30 minutes in electric resistance furnace preheated to a temperature of 900 °C. Heating rate over 300 °C/min was reached by direct insertion of the sample to heated furnace. After SHS process, the ampoules with the samples were air-cooled to laboratory temperature.

A part of the prepared samples was cut off using precision metallographic diamond saw and used for microstructure characterization and the rest was milled in vibrating laboratory mill VM4 for 7 minutes. Resulting powder was consolidated by the means of Spark Plasma Sintering at the temperature of 1100 °C for 5 min using the heating rate of 100 °C/min and pressure of 48 MPa. Formed cylindrical samples had diameter of about 20 mm and height of approx. 5 mm.

2.3. Method of investigation and sample preparation

For the microstructure inspections, samples were ground by P80 to P4000 sandpapers (abrasive particles Al₂O₃ and SiC) and polished by diamond paste D2. After that, the samples were etched by Kroll's agent (10 ml HF, 5 ml HNO₃ and 50 ml H₂O). Microstructure was investigated by the metallographic optical microscope Olympus PME3 and was documented using the digital camera Carl Zeiss AxioCam ICc3 and AxioVision software. Porosity was evaluated using Lucia 4.8 image analyser. The electron microscope TESCAN VEGA 3 LMU equipped with EDS analyser (SEM-EDS) was used for more detailed view of the structure and identification of present phases.

TEM thin discs were mechanically grinded and thinned to a final thickness of 80-90 µm, then punched and dimpled in both sides to a thickness of about 30 µm. Finally, TEM discs were ion milled by a Gatan[®] PIPS working at 8 KeV, with incident beam angle, respectively, of 8, 6, and 4° for a total preparation time of less than 30 min. TEM inspections were carried out using a Philips CM-20 working at 200 KeV, and using a double-tilt specimen holder. TEM inspections were performed for the TiAl15Si15 and TiAl10Si20 intermetallic alloys.

Mechanical tests were performed on the compact samples. Tests of compressive strength were conducted by the means of the testing machine LabTest 5.250SP1-VM. Values of yield strength in compression were

determined from the measured loading curves. Vickers hardness with a load of 5 kg (HV 5) was measured from 10 indentions into the polished samples (10 measurements were made on each specimen).

Fracture toughness was measured by Vickers indentation method on microhardness tester Future-Tech FM-700. Vickers hardness with a load of 1 kg (HV 1, 9.8 N) was measured from 10 indentions into the polished sample. Indentions were observed with optical microscope Olympus PME3. Fracture toughness was calculated through Palmquist's equation (1):

$$Kc = 0,016 \cdot \left(\frac{E}{HV}\right)^{1/2} \cdot \left(\frac{F}{c^{3/2}}\right) \quad (1)$$

where E is modulus of elasticity [GPa], HV is Vickers hardness [GPa], F is load [N] and c is half of the crack length after indentation [mm] (Fig. 1) [15].

Abrasive wear resistance was tested by modified pin-on-disc method on tribometer at room temperature. The sample was moving on rotating sandpaper P1200 with load 5.8 N for 15 minutes. Grinding distance was approximately 2.5 km long. Wear rate was calculated through equation (2):

$$w = \frac{\Delta m}{\rho \cdot l} \quad (2)$$

where w is wear rate [$\text{cm}^3 \cdot \text{m}^{-1}$], Δm is the weight lost [g], ρ is density of alloy [$\text{g} \cdot \text{cm}^{-3}$] a l is length of grinding distance on sandpaper [m]. The average density of Ti-Al-Si alloys ($4.7 \text{ g} \cdot \text{cm}^{-3}$) was measured by Archimedes method.

Nanoindentation measurements were carried out on samples polished up to a $0.25 \text{ } \mu\text{m}$ diamond paste. Measurements were performed on a Hisytron[®] Inc. UBI-1[®] Triboscope nanoindenter, using a sharp (radius $\sim 160 \text{ nm}$) diamond Berkovich tip. Tip area function calibration was obtained by indentation on a fused quartz sample, according to the calibration procedure outlined in [M1]. Unload curve analysis was done according to the Oliver and Pharr method [M2]. To determine the hardness, H , and reduced elastic modulus, E_r , a trapezoidal load function (5s load – 15 s hold – 5 s unload) was used.

3. Results and discussion

3.1. Alloys after SHS

Based on a previous published paper by Knaislová et al. [16], Ti-Al-Si samples were pressed from powders using universal loading machine and SHS process was carried out in electric resistance furnace in silica glass ampoules at 900 °C for 30 min. All prepared alloys (TiAl10Si20, TiAl10Si30, TiAl15Si15, TiAl20Si20, TiAl20Si30 and TiAl30Si20) have very porous structure. Phase composition is shown by XRD patterns in Fig. 2 and corresponding microstructures in Fig.3.

In the case of TiAl10Si20 and TiAl15Si15 alloys, containing the mixture of TiAl and Ti_5Si_3 phases, the phase composition corresponds well to the equilibrium phase diagram of Ti-Al-Si system (Table 1) [17]. These alloys, TiAl10Si20 (Fig. 3a) and TiAl15Si15 (Fig. 3c), are characterized by a very homogenous structure with fine sharp-edged Ti_5Si_3 silicides and TiAl matrix (Fig. 2). Also the phase composition of TiAl30Si20 alloy ($TiSi$, Ti_5Si_4 , $TiAl_3$) follows the Ti-Al-Si equilibrium phase diagram (Fig.4, Table 1). In TiAl15Si15, traces of $TiSi$ silicide were also detected. In the case of TiAl20Si20, TiAl10Si30 and TiAl20Si30 there are deviations from the equilibrium phase composition due to minor amounts of unreacted silicon. Due to the residual initial component, the other phases also differ from the equilibrium state. The alloy TiAl20Si20 is composed of silicides Ti_5Si_3 , Ti_5Si_4 and $TiSi_2$, while the higher proportion of aluminium to titanium unbound in silicides results in the single-phase $TiAl_3$ matrix (Fig. 2). TiAl10Si30 (Fig. 3b) alloy has a heterogeneous structure and contains a highly branched and angular silicides Ti_5Si_3 , in whose edges the $TiSi$ silicide is located (Fig. 2). TiAl30Si20 (Fig. 3f) alloy contains large sharp-edged particles of Ti_5Si_4 silicide surrounded by $TiSi$ silicide.

The reasons for the deviations from the equilibrium phase composition can be probably caused by too short duration of the process or by highly exothermic nature of the reactions. Due to rapid evolution of the heat during the reaction, the sample heats rapidly. When the reaction is completed, the temperature drops quickly to the furnace temperature. Therefore, the aluminide and silicide phases are supersaturated by silicon or aluminium, respectively. This fact was proved by EDS local chemical analysis, see Table 2.

Area fraction of silicides in alloys was determined from images of microstructure acquired by the optical microscope. The samples after SHS were used, because there were clearly visible differences between the phases and it can be highly expected that the volume fraction of silicides is not affected by subsequent milling and SPS sintering significantly. Manual image analysis using grid method was applied for the determination of the area fraction of silicides. In Fig. 4 is shown that the largest fraction of silicides is in the

TiAl10Si30 and TiAl20Si30 alloys, which corresponds to the highest silicon content in the starting powders. The lowest amount of silicides was found in the TiAl15Si15 alloys, which has homogenous fine-grained structure formed by aluminides and silicides nearly in the same ratio (the area fraction of silicides is 55 vol. %).

The main problem of the alloys prepared by this process is a porous structure (Fig. 5). For this reason, we included milling in a vibratory mill after SHS and Spark Plasma Sintering for subsequent consolidation of the milled powder. It was aimed at formation of homogenized structure with low porosity.

3.2. Alloys after consolidation by SPS

After Spark Plasma Sintering at the temperature of 1100 °C, Ti-Al-Si alloys are characterised by a nearly nonporous fine-grained structure. Phase composition is shown in Fig.6.

Microstructure of SPS consolidated samples (Fig. 7, Fig. 8) is composed of silicides (lighter areas) and aluminides (darker areas). The phase composition of TiAl10Si20 and TiAl30Si20 remained unchanged by SPS (Table 2) due the fact that the equilibrium phase composition was achieved already after SHS. The TiAl15Si15 is characterised, as after SHS, by the most fine-grained structure with Ti_5Si_3 silicides in TiAl matrix. The traces of TiSi disappeared as a result of the homogenization of the material during thermal exposure in SPS device. However, in the case of the other alloys (TiAl10Si30, TiAl20Si20 and TiAl20Si30), the thermal exposure during SPS was not sufficient to achieve the equilibrium phase composition, even though some minor changes proceeded, see Table 2. The substitution of elements in aluminide and silicide phase by silicon and aluminium, respectively, stays at similar level as after SHS (Table 3). It confirms that the diffusion-controlled processes leading to the phase composition changes during SPS were only minimal.

Consolidated alloys prepared by Spark Plasma Sintering method are characterised by low porosity in comparison with alloys prepared by SHS. Porosity of each alloy does not exceed the value of 2.5 % by volume (Fig. 5).

Concurrently, they exhibit finer-grained structure than directly after SHS. This fact is caused by cracking of brittle silicides during milling.

3.3 Mechanical and tribological properties of Ti-Al-Si alloys after consolidation by SPS

Hardness of Ti-Al-Si alloys (Fig. 9) varies between 630 and 1100 HV 5 and increases with the growing amount of silicon in alloy. TiAl10Si30 and TiAl20Si30 alloys achieve the highest hardness. It is because silicon in alloy supports formation of higher amount of silicides (Ti_5Si_3 , Ti_5Si_4 and TiSi), that have the higher hardness than present aluminides [7]. The hardness of the Ti-Al-Si alloys reaches the level of cold-work tool steels (e.g. Vanadis 6) [18]. However, heat treatment is required for tool steels to reach this value of hardness. In the case of tested Ti-Al-Si alloys, no heat treatment was required.

Fig. 10 shows representative nanoindentation load-displacement curves of the five following intermetallic compounds: TiAl10Si20, TiAl10Si30, TiAl15Si15, TiAl20Si20, TiAl20Si30. It appeared that the TiAl15Si15 is the one with the deepest penetration depth (being up to 450 nm), and the TiAl20Si20 is the one showing the lowest penetration depth of 90 nm. This, in turns, reflects a significant difference in the mean hardness values obtained for the five different intermetallic alloys. With this respect, Fig. 11 shows a histogram of hardness, H , and local elastic modulus, E_r . It resulted that as the Ti volume fraction of the intermetallic alloy decreases in favour of the aluminum and silicon content, the hardness and elastic modulus tend to rise. Thus, the lowest value of ~ 1 GPa, of the TiAl15Si15 alloy, keeps to increase to ~ 4.5 and ~ 7 GPa, in the TiAl10Si30 and TiAl20Si30 alloy, respectively. The only clear exception is constituted by the TiAl20Si20 alloy that shows a remarkable high value of hardness with a rather modest local elastic modulus. These data suggest a larger stiffness of the TiAl20Si20 compound, respect to the other 5 intermetallic alloys.

Fracture toughness of Ti-Al-Si alloys is shown in Fig. 12. All of the alloys achieve low values of fracture toughness (from 0.7 to 1.7 $\text{MPa}\cdot\text{m}^{1/2}$) compared to Ti-Al-Si alloys prepared by mechanical alloying [19]. These values are lower than for brittle ceramics - alumina or silicon carbide, which reach the values of fracture toughness around 4 $\text{MPa}\cdot\text{m}^{1/2}$ [20]. It implies that further improvement is required, for example by refinement of the structure. The showed TiAl20Si20 worst fracture toughness response is also supported by the obtained large stiffness and quite high hardness values by nanoindentation.

Abrasive wear resistance is shown in Fig. 13. TiAl15Si15 alloy contains large amount of softer aluminides and the lowest fraction of hard silicides among all tested alloys (Fig. 4). Therefore, this alloy reaches the highest abrasive wear rate, i.e. the lowest abrasive wear resistance. TiAl10Si20 alloy manifests the highest abrasive wear resistance (i.e. the lowest wear rate), which is due to combination of three factors: very fine-grained structure, presence of TiAl (aluminide with good ductility, more ductile than TiAl_3) and

higher portion of silicides (Ti_5Si_3). Abrasive wear resistance of tested alloys is comparable (or even slightly higher) with high grade cold-work tool steels (e.g. Vanadis 6) [21,22].

3.4. TEM inspections of the TiAl15Si15 and TiAl10Si20 alloys.

Fig. 14 shows representative BF-TEM micrographs of the TiAl15Si15 and TiAl10Si20 alloy microstructure. In particular, Fig. 14a shows the TiAl15Si15 alloy grain structure in the [001] crystallographic direction, while Fig. 14b reports the grained structure in the [01-12] hexagonal crystallographic direction. Actually, the reported XRD results on the SPS- TiAl15Si15 revealed the presence of two phases: Ti_5Si_3 , which is hexagonal with $\text{P6}_3/\text{mcm}$ Hermann-Mauguin lattice space notation, and TiAl , which is tetragonal with $\text{P4}/\text{mmm}$ Hermann-Mauguin lattice space notation. Thereafter, Fig. 14a refers to the grained structure of the tetragonal TiAl phase, while Fig. 14b refers to the hexagonal Ti_5Si_3 phase. Fig. 14c and 14d refers to the TiAl10Si20 alloy, in which the XRD analyses revealed the presence of the same two phases: Ti_5Si_3 and TiAl . In this case, Fig. 14c reports the tetragonal [011] crystal orientation, and thus refers to the TiAl phase, while Fig. 3d shows the microstructure of the TiAl10Si20 alloy taken at [-2110] crystal orientation, thus preferentially showing the microstructure of the Ti_5Si_3 phase.

It appeared that the grained structure of the TiAl15Si15 alloy is much finer and regular respect to the TiAl10Si20 . The mean grain size of the TiAl15Si15 was $320 \pm 20 \mu\text{m}$ (equivalent diameter), practically for both the phases of which the alloy is constituted. On the contrary, the mean grain size of the TiAl10Si20 was significantly higher, as it was evaluated that the Ti_5Al_3 phase had a mean equivalent diameter of $1100 \pm 150 \mu\text{m}$, and the TiAl phase of $950 \pm 100 \mu\text{m}$. That is, the TiAl10Si20 alloy grained structure was 3-times coarser than the TiAl15Si15 alloy. Moreover, the microstructure of the SPS- TiAl15Si15 appeared to be more homogeneous, and the TiAl10Si20 grained microstructure is decorated by a large quantity of mutually orthogonal twinning.

According to the histograms of Fig. 4 and Fig. 5, the TiAl15Si15 alloy after SPS, resulted to be the one with lowest fraction of silicides, and, more important, the one with lowest porosity. TEM inspections revealed that this intermetallic alloy was able to retain its homogeneity and fine structure after the SPS consolidation process. On the other hand, the showed difference of fracture toughness (Fig. 12) and wear resistance (Fig. 13) of the two alloys: TiAl15Si15 and TiAl10Si20 is likely to be related not only to a

different efficiency of the consolidation process in terms of intermetallic composition, but it is also related to the significant microstructure differences observed by TEM (Fig. 14).

4. Conclusion

Microstructure of Ti-Al-Si alloys is very porous after SHS. TiAl₂₀Si₂₀ and TiAl₃₀Si₂₀ alloys are characterised by TiAl₃ matrix and TiAl₁₀Si₃₀ contained Ti₂Al aluminide phase unlike other alloys with TiAl matrix. All alloys contain various combinations of silicides Ti₅Si₃, Ti₅Si₄ and TiSi. The coincidence with the equilibrium phase diagram was relatively good, when taking into account the short period of the SHS process and rapid temperature changes. TiAl₁₀Si₂₀ and TiAl₁₅Si₁₅ alloys have the most fine-grained structure.

Spark Plasma Sintering was used for the consolidation of milled powders after SHS. There were only minor changes in the phase composition of the alloys during SHS, forwarding closer to the equilibrium state. Microstructure of compacted Ti-Al-Si alloys is almost non-porous. Therefore, this method is useful for preparation of intermetallic based on the Ti-Al-Si system.

The alloys achieve good mechanical properties except for the fracture toughness. For the applications, where high hardness is necessary, the best alloys are with the highest amount of silicon and with large portion of silicides (TiAl₁₀Si₃₀ and TiAl₂₀Si₃₀). All Ti-Al-Si alloys reach low values of fracture toughness, they are very brittle because of high amount of silicides in the structure. The abrasive wear resistance is very good, especially in the case of TiAl₁₀Si₂₀ alloy, and it is comparable with high grades of cold-work tool steels. The nanoindentation results showed that hardness appeared to rise as the content of Al and Si in the Ti-based intermetallic increase. The highest stiffness of the TiAl₂₀Si₂₀, showed by the combined measured very high hardness and relatively low elastic modulus, resulted in a high fracture toughness of this intermetallic alloy.

The mechanical results were fully supported by the microstructure differences observed in two of the five here presented intermetallic alloys, namely, the TiAl₁₅Si₁₅ and TiAl₁₀Si₂₀.

Acknowledgement

This research was financially supported by Czech Science Foundation, project No. P108/12/G043.

References

- [1] F. Yang, F.T. Kong, Y.Y. Chen, S.L. Xiao, Effect of spark plasma sintering temperature on the microstructure and mechanical properties of a Ti₂AlC/TiAl composite, *Journal of Alloys and Compounds*, 496 (2010) 462-466.
- [2] K.P. Rao, J.B. Zhou, Characterization of mechanically alloyed Ti–Al–Si powder blends and their subsequent thermal stability, *Materials Science and Engineering: A*, 338 (2002) 282-298.
- [3] Y. Mishin, C. Herzig, Diffusion in the Ti–Al system, *Acta Materialia*, 48 (2000) 589-623.
- [4] P. Novák, J. Kříž, F. Průša, J. Kubásek, I. Marek, A. Michalcová, M. Voděrová, D. Vojtěch, Structure and properties of Ti–Al–Si–X alloys produced by SHS method, *Intermetallics*, 39 (2013) 11-19.
- [5] Z.Q. Guan, T. Pfullmann, M. Oehring, R. Bormann, Phase formation during ball milling and subsequent thermal decomposition of Ti–Al–Si powder blends, *Journal of Alloys and Compounds*, 252 (1997) 245-251.
- [6] J.S. Wu, P.A. Beaven, R. Wagner, The Ti₃(Al, Si) + Ti₅(Si, Al)₃ Eutectic Reaction in the Ti–Al–Si system, *Scripta Metallurgica et Materialia*, 24 (1990) 207-212.
- [7] P. Novák, A. Michalcová, J. Šerák, D. Vojtěch, T. Fabián, S. Randáková, F. Průša, V. Knotek, M. Novák, Preparation of Ti–Al–Si alloys by reactive sintering, *Journal of Alloys and Compounds*, 470 (2009) 123-126.
- [8] D.E. Alman, Reactive sintering of TiAl–Ti₅Si₃ in situ composites, *Intermetallics*, 13 (2005) 572-579.
- [9] L. Zemčík, A. Dlouhý, S. Król, M. Prazmowski, Vacuum Metallurgy of TiAl Intermetallics, *Metal*, (2005).
- [10] A. Lasalmonie, Intermetallics: Why is it so difficult to introduce them in gas turbine engines?, *Intermetallics*, 14 (2006) 1123-1129.
- [11] K. Morsi, Review: reaction synthesis processing of Ni–Al intermetallic materials, *Materials Science and Engineering: A*, 299 (2001) 1-15.
- [12] S.A. Tsukerman, INTRODUCTION, in: *Powder Metallurgy*, Pergamon, 1965, pp. vii-xi.
- [13] Z.-H. Zhang, Z.-F. Liu, J.-F. Lu, X.-B. Shen, F.-C. Wang, Y.-D. Wang, The sintering mechanism in spark plasma sintering – Proof of the occurrence of spark discharge, *Scripta Materialia*, 81 (2014) 56-59.

- [14] M. Suárez, A. Fernández, J.L. Menéndez, R. Torrecillas, H.U. Kessel, J. Hennicke, R. Kirchner, T. Kessel, Challenges and Opportunities for Spark Plasma Sintering: A Key Technology for a New Generation of Materials, InTech, (2013).
- [M1] M. Cabibbo, P. Ricci, R. Cecchini, Z. Rymuza, J. Sullivan, S. Dub, S. Cohen, An international round-robin calibration protocol for nanoindentation measurements, *Micron*, 43 (2012) 215-222.
- [M2] W.C. Oliver, G.M. Pharr, Measurement of hardness and elastic modulus by instrumented indentation: Advances in understanding and refinements to methodology, *J. Mater. Res.*, 19 (2004) 3-15.
- [15] J. Vystrčil, Příprava intermetalických fází v systémech Fe-Al-Si a Ti-Al-Si mechanickým legováním, in: ÚKMKI, VŠCHT, Praha, 2014.
- [16] A. Knaislová, P. Novák, F. Průša, Preparation of Ti-Al-Si alloys by powder metallurgy, *Manufacturing Technology*, 16 (2016) 1274-1278.
- [17] Al-Si-Ti (Aluminium - Silicon - Titanium), in: G. Effenberg, S. Ilyenko (Eds.) *Light Metal Systems. Part 4: Selected Systems from Al-Si-Ti to Ni-Si-Ti*, Springer Berlin Heidelberg, Berlin, Heidelberg, 2006, pp. 1-15.
- [18] J. Ptacinova, P. Jurci, I. Dlouhý, Fracture toughness of ledeburitic Vanadis 6 steel after sub-zero treatment for 17 h and double tempering, *Materiali in Tehnologije*, 51 (2017) 729-733.
- [19] J. Vystrčil, P. Novák, A. Michalcová, Preparation of Ultra-Fine Grained Alloys Based on Fe-Al-Si And Ti-Al-Si Intermetallic Compounds by Powder Metallurgy Using the Mechanical Alloying, *Manufacturing Technology*, Vol. 15 (2015) 238-242.
- [20] W.C. Wagner, T.M. Chu, Biaxial flexural strength and indentation fracture toughness of three new dental core ceramics, *The Journal of Prosthetic Dentistry*, 76 (1996) 140-144.
- [21] P. Jurci, J. Sobotová, P. Salabová, O. Prikner, B. Šuštaršič, D. Jenko, Subzero treatment of P/M Vanadis 6 ledeburitic tool steel, *International Heat Treatment and Surface Engineering*, 7 (2013) 125-128.
- [22] J. Sobotova, P. Jurci, I. Dlouhy, The effect of subzero treatment on microstructure, fracture toughness, and wear resistance of Vanadis 6 tool steel, *Materials Science and Engineering: A*, 652 (2016) 192-204.

Table and Figure captions

Table 1. Comparison of phase composition of Ti-Al-Si alloys in phase diagram [17], after SHS and after SPS

Table 2: Average composition of present phases after SHS

Table 3: Average composition of present phases after SPS

Fig. 1. Scheme of the fracture toughness measurement by indentation method

Fig. 2. XRD patterns of samples prepared by SHS at 900 °C for 30 min.

Fig. 3. Microstructure of a) TiAl10Si20, b) TiAl10Si30, c) TiAl15Si15, d) TiAl20Si20, e) TiAl20Si30, f) TiAl30Si20 prepared by SHS at 900 °C for 30 min in electric resistance furnace with the heating rate of 300 °C/min.

Fig. 4. Area fraction of silicides in Ti-Al-Si alloys after SPS

Fig. 5. Porosity after SHS and SPS of Ti-Al-Si alloys

Fig. 6. XRD patterns of samples prepared by SPS at 1100 °C for 5 min.

Fig. 7. Microstructure of a) TiAl10Si20, b) TiAl10Si30, c) TiAl15Si15, d) TiAl20Si20, e) TiAl20Si30, f) TiAl30Si20 prepared by SPS at 1100 °C for 5 min using the heating rate of 100 °C/min and pressure of 48 MPa

Fig. 8. Detailed microstructure of a) TiAl10Si20, b) TiAl10Si30, c) TiAl15Si15, d) TiAl20Si20, e) TiAl20Si30, f) TiAl30Si20 prepared by SPS at 1100 °C for 5 min using the heating rate of 100 °C/min and pressure of 48 MPa

Fig. 9. Hardness of Ti-Al-Si alloys prepared by SPS at 1100 °C.

Fig. 10. Load-displacement representative curves of the different phases detected in the intermetallic alloys.

Fig. 11. Histogram of hardness, H , and local elastic modulus, E_r , of the TiAl10Si20, TiAl10Si30, TiAl15Si15, TiAl20Si20, TiAl20Si30 intermetallic alloys.

Fig. 12. Fracture toughness of Ti-Al-Si alloys prepared by SPS at 1100 °C

Fig. 13. Abrasive wear rate of Ti-Al-Si alloys prepared by SPS at 1100 °C

Fig. 14. TEM micrographs of the TiAl15Si15 alloy (mechanically alloyed for 4h, SPS at 80MPa 100°C/15min, cooled at 50°C/min), a) ZA [001] preferentially showing TiAl grains, and b) [01-12] preferentially showing Ti₅Si₃ grains; TiAl10Si20 alloy (SPS at 48MPa, 1200°C/15min, cooled at 50°C/min), c) ZA [011] preferentially showing TiAl grains, and c) [-2110] preferentially showing Ti₅Si₃ grains.

Table 1.

Alloy	Phase diagram	SHS	SPS
TiAl10Si20	Ti ₅ Si ₃ , TiAl	Ti ₅ Si ₃ , TiAl	Ti ₅ Si ₃ , TiAl
TiAl10Si30	TiSi, Ti ₅ Si ₄ , TiAl ₃	TiSi, Ti ₅ Si ₃ , Ti ₅ Si ₄ , Ti ₂ Al, Si	TiSi, Ti ₅ Si ₃ , TiAl ₃ , Ti ₂ Al, Si
TiAl15Si15	Ti ₅ Si ₃ , TiAl	Ti ₅ Si ₃ , TiAl, TiSi	Ti ₅ Si ₃ , TiAl
TiAl20Si20	Ti ₅ Si ₃ , TiAl ₃	Ti ₅ Si ₃ , TiAl ₃ , Ti ₅ Si ₄ , TiSi ₂ , Si	Ti ₅ Si ₃ , TiAl ₃ , Ti ₅ Si ₄ , TiSi ₂
TiAl20Si30	TiSi, TiSi ₂ , TiAl ₃	TiSi, Ti ₅ Si ₃ , TiAl, Ti ₂ Al, Ti ₅ Si ₄ , Si	Ti ₅ Si ₃ , TiAl, Ti ₅ Si ₄ , Si
TiAl30Si20	TiSi, Ti ₅ Si ₄ , TiAl ₃	TiSi, Ti ₅ Si ₄ , TiAl ₃	TiSi, Ti ₅ Si ₄ , TiAl ₃

Table 2.

at. %	Ti	Al	Si
TiAl	51 ± 3	40 ± 5	10 ± 3
TiAl ₃	29 ± 3	59 ± 5	12 ± 2
Ti ₅ Si ₃	64 ± 3	9 ± 4	28 ± 4
TiSi	53 ± 2	2 ± 2	46 ± 3

Table 3.

at. %	Ti	Al	Si
TiAl	50 ± 3	42 ± 5	9 ± 3
TiAl ₃	30 ± 3	55 ± 5	12 ± 2
Ti ₅ Si ₃	63 ± 3	8 ± 4	29 ± 4
TiSi	50 ± 2	4 ± 3	44 ± 3

Figure 1.

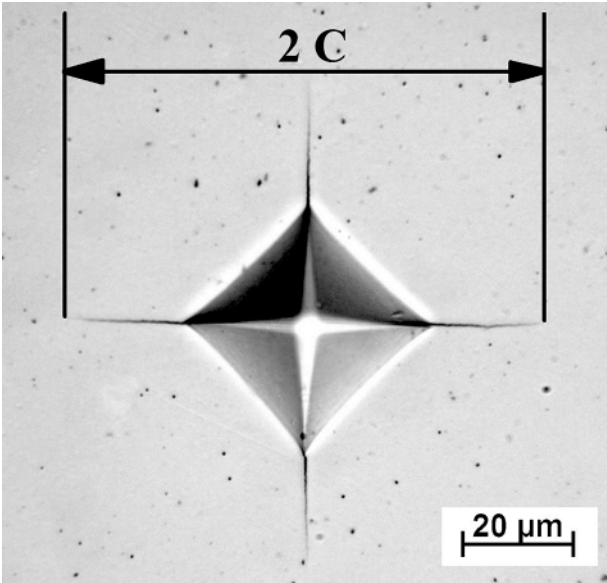
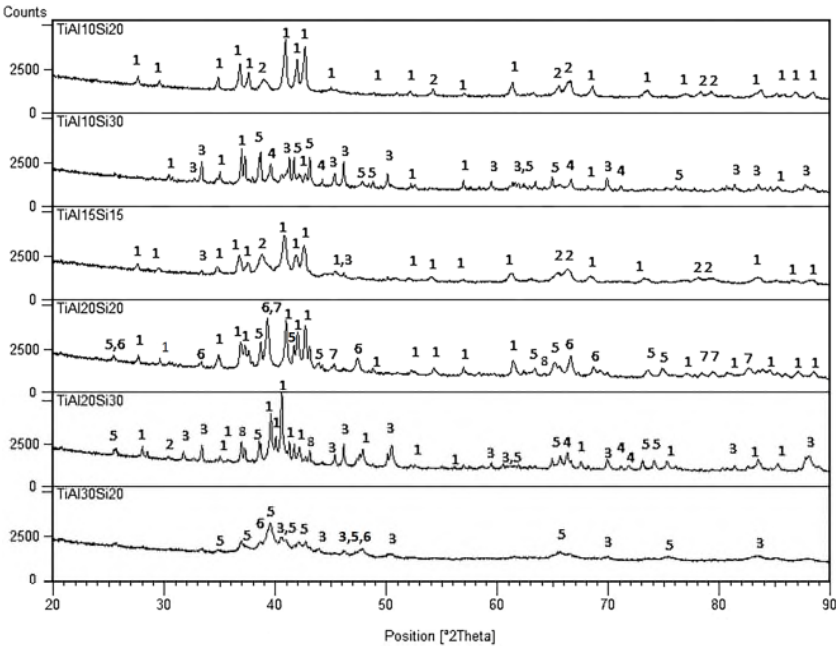


Figure 2.



1	2	3	4	5	6	7	8
Ti ₅ Si ₃	TiAl	TiSi	Ti ₂ Al	Ti ₅ Si ₄	TiAl ₃	TiSi ₂	Si

Figure 3.

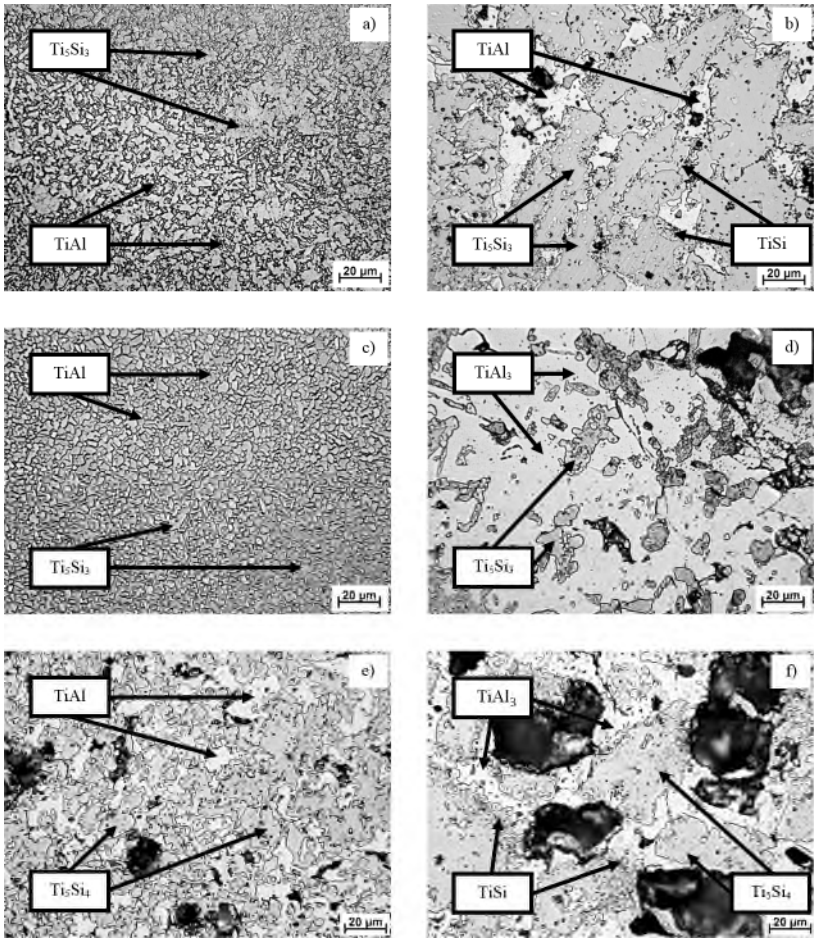


Figure 4.

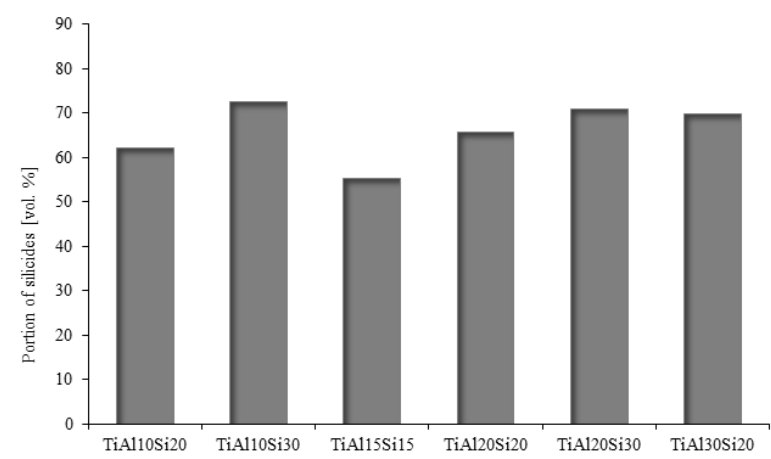


Figure 5.

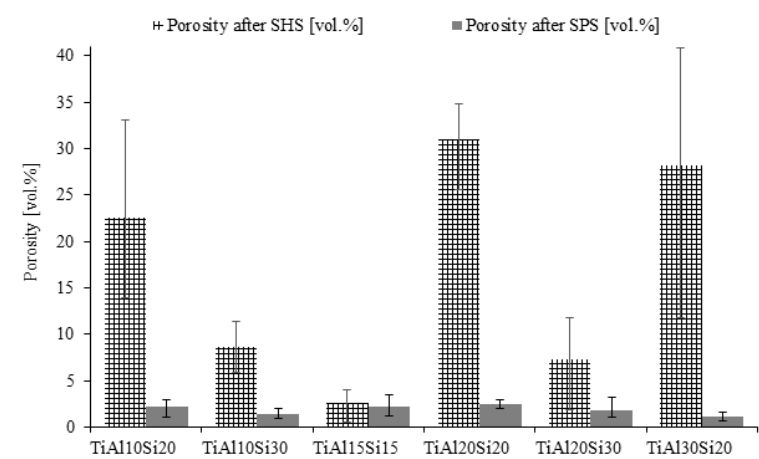
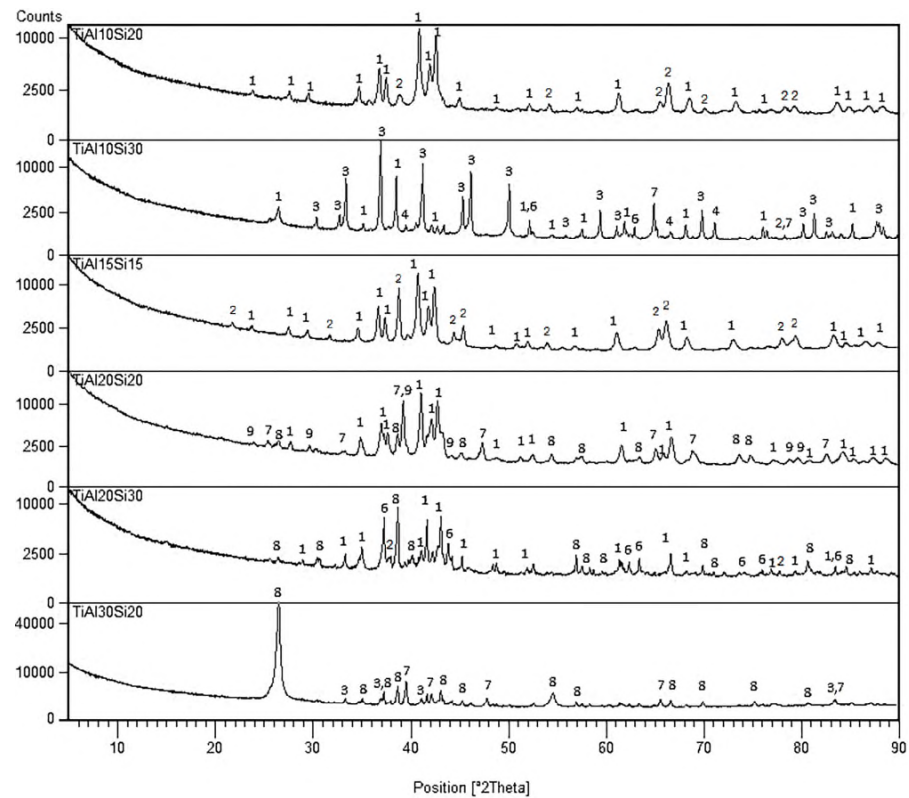


Figure 6.



1	2	3	4	5	6	7	8	9
Ti ₅ Si ₃	TiAl	TiSi	Ti ₂ Al	Ti ₃ Al	Si	TiAl ₃	Ti ₅ Si ₄	TiSi ₂

Figure 7.

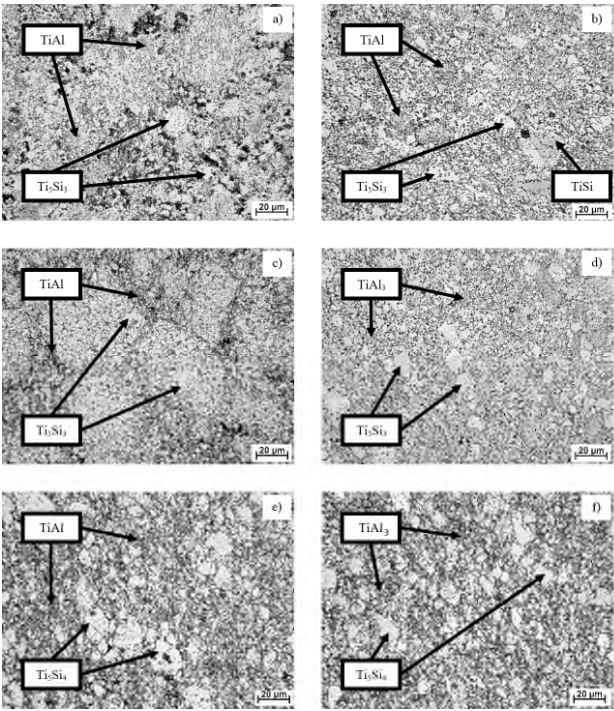


Figure 8.

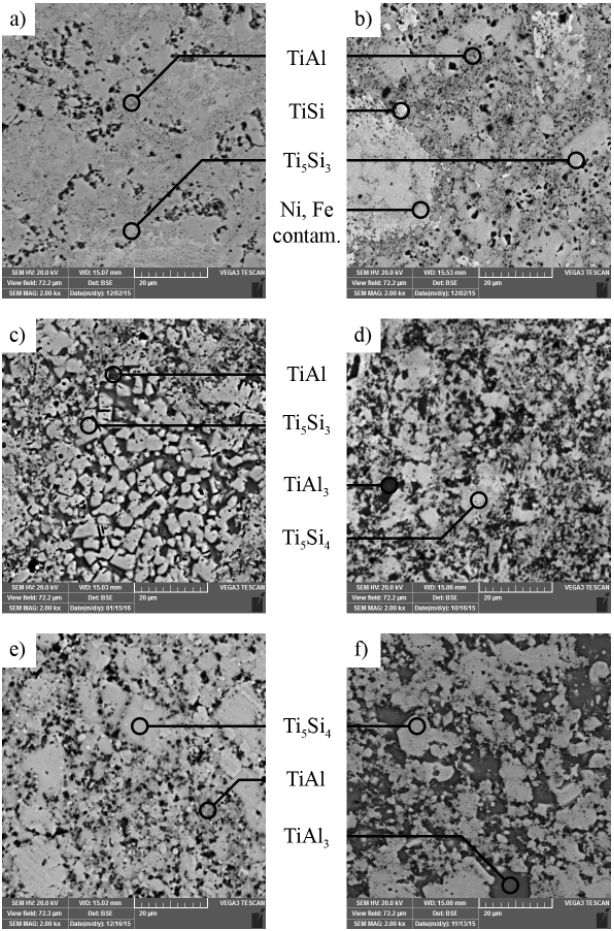


Figure 9.

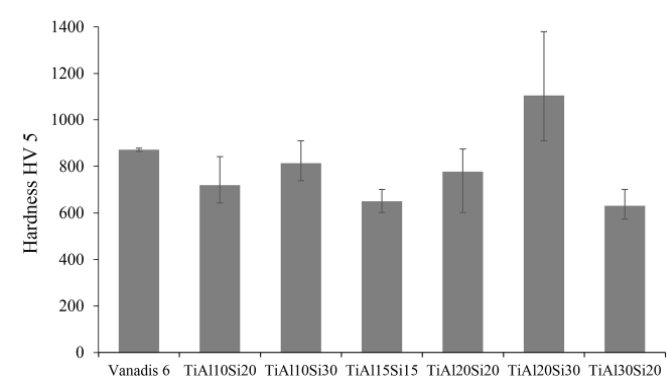


Figure 10.

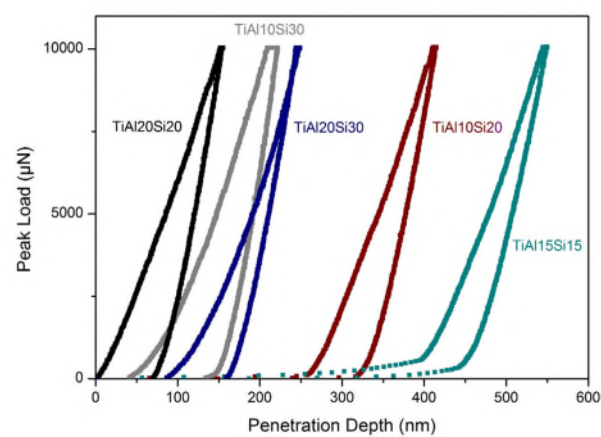


Figure 11.

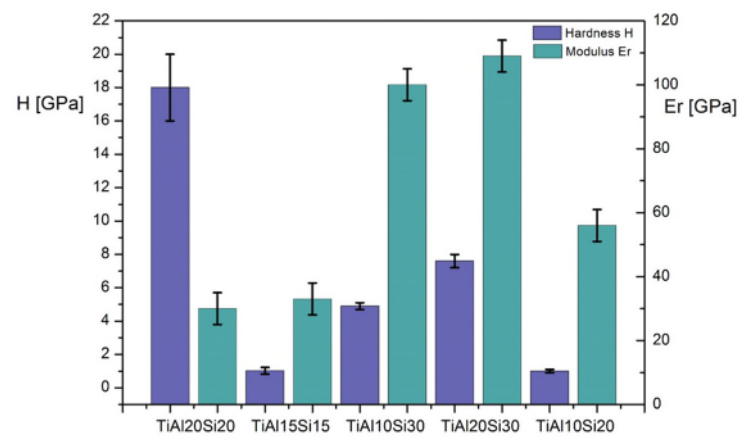


Figure 12.

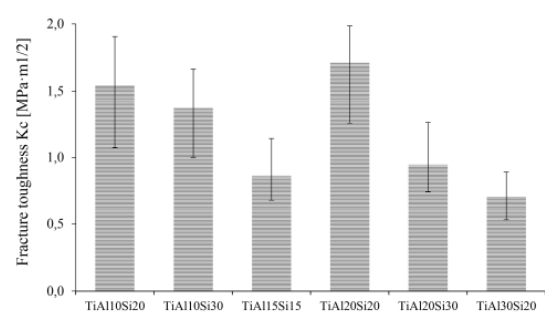


Figure 13.

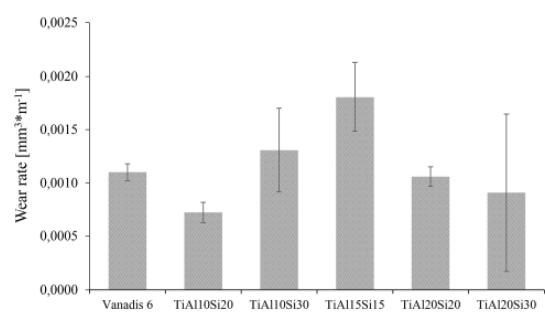


Figure 14.

